



Modeling and compensation of volumetric errors for five-axis machine tools



Sitong Xiang^a, Yusuf Altintas^{b,*}

^a School of Mechanical Engineering, Shanghai Jiao Tong University, 800 Dong Chuan Road, Shanghai 200240, PR China

^b Manufacturing Automation Laboratory, Department of Mechanical Engineering, The University of British Columbia, Vancouver, BC, Canada, V6T 1Z4

ARTICLE INFO

Article history:

Received 10 August 2015

Received in revised form

4 November 2015

Accepted 11 November 2015

Available online 1 December 2015

Keywords:

Five-axis machine tool

Volumetric error

Error measuring

Error compensation

Screw theory

ABSTRACT

This article proposes a method to measure, model and compensate both geometrically dependent and independent volumetric errors of five-axis, serial CNC machine tools. The forward and inverse kinematics of the machine tool are modeled using the screw theory, and the 41 errors of all 5 axes are represented by error motion twists. The component errors of translational drives have been measured with a laser interferometer, and the errors of two rotary drives have been identified with ballbar measurements. The complete volumetric error model of a five-axis machine has been modeled in the machine's coordinate system and proven experimentally. The volumetric errors are mapped to the part coordinates along the tool path, and compensated using the kinematic model of the machine. The compensation strategy has been demonstrated on a five-axis machine tool controlled by an industrial CNC with a limited freedom, as well as by a Virtual CNC which allows the incorporation of compensating all 41 errors.

© 2015 Elsevier Ltd. All rights reserved.

1. Introduction

There are 21 known geometric errors in three-axis machine tools [1], and 41 errors exist for five-axis serial machine tools. The errors have integrated effects in determining the orientation and position errors of the tool tip relative to the workpiece in five axis machine tools. The modeling and compensation of these volumetric errors are needed to improve the accuracy of the machine in the five-axis machining of parts [2].

The volumetric error compensation of multi-axis machine tools has 3 engineering steps: the kinematic modeling, measurement and modeling of axis errors, and their compensation during the positioning of the machine along the tool path. The kinematics of the machine have been modeled by applying the homogeneous transformation matrix (HTM) [1], by using the screw theory [3,4], by the product of exponential model [5], or by the differentiable manifold-based method [6]. This paper adopts the screw theory-based, generalized modular kinematic model of the five-axis machines reported previously [3].

The geometric errors of machine axes are measured by direct and indirect methods as reviewed by Schwenke [7] and Ibaraki [8]. The laser interferometer is mostly used in measuring the geometric errors of translational axes directly, and the geometric

errors of rotary axes are identified indirectly by measurements with a ballbar [9], *R*-test [10,11], touch trigger probe [12,13], machining tests [14] and tracking interferometer [15,16]. Once the geometric errors of the axes are measured and modeled as a function of position in the Machine Coordinate System (MCS), they are translated to the tool orientation and tool tip position using a forward kinematic model of the machine in the Part Coordinate System (PCS). The errors are compensated by transforming the tool position and orientation errors to drive components via the inverse kinematic model of the machine in PCS. Lei and Hsu [17] presented a compensation algorithm for five-axis machine tools and analyzed the singularity problems. They [18] compensated the tool axis orientation errors first, followed by the compensation of the translational errors. Zhu [19] presented an identification approach for recognizing 6 error parameters of rotary axes via the ballbar test and verified the compensation of a five-axis machine tool on a “S” shape tool path. Huang [20] merged an iterative compensation method into the post-processor and generated a new, error-compensated NC program.

Commercial CNC systems have look-up tables which can be filled with axis errors at each position of the machine within its operating volume. However, they allow for the compensation of only translational errors, but not the deviations of tool orientations needed in five-axis machining applications [7].

This paper presents a detailed modeling, measurement and compensation method for the volumetric errors of five-axis machine tools as outlined in the flow chart given in Fig. 1. Yang et al. [21] used the screw theory to identify and compensate the 11

* Corresponding author.

E-mail addresses: stone.xiangst@gmail.com, xiangst@sjtu.edu.cn (S. Xiang), altintas@mech.ubc.ca (Y. Altintas).

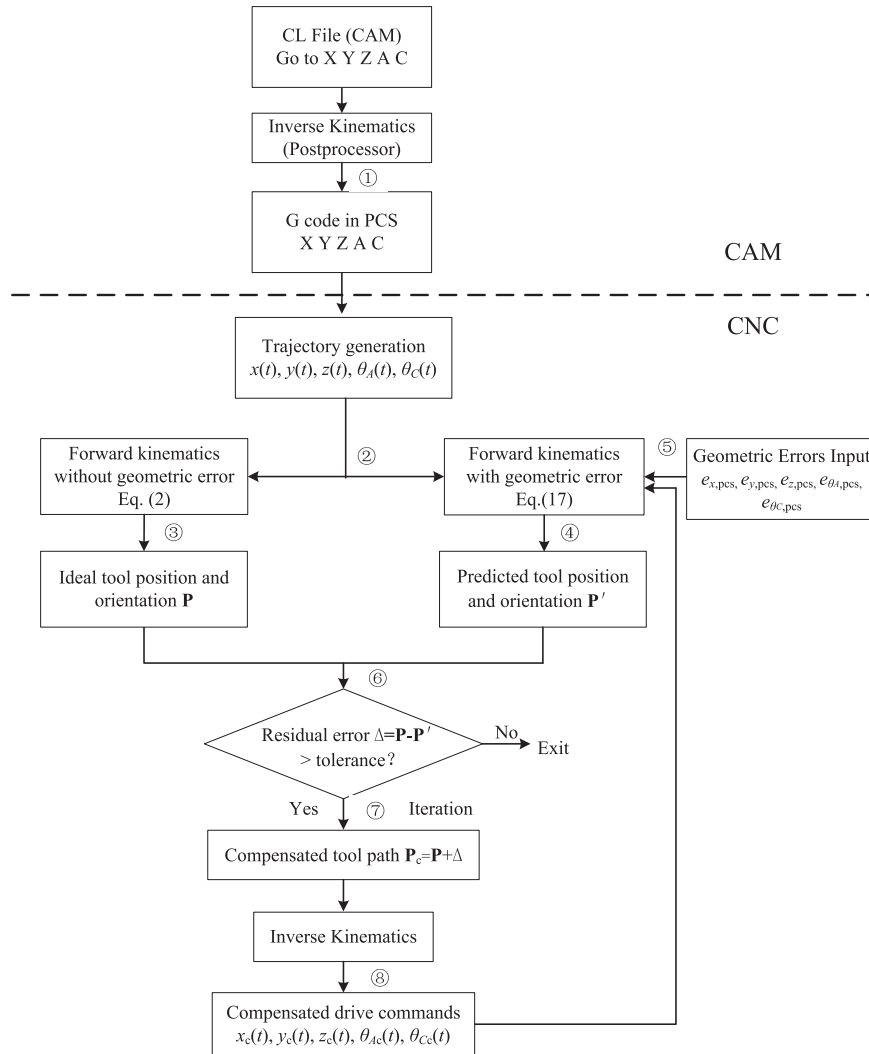


Fig. 1. Flowchart of compensation strategy.

position-independent geometric errors (PIGEs), i.e., the squareness of 3 translational axes and 4 linear offsets and 4 angular tilts of two rotary axes. This article extends Yang's method [21] by including both position-dependent and position-independent 41 geometric errors with a proposed, unified compensation method with the introduction of error twists.

Henceforth, the paper is organized to present the measurement, modeling and compensation algorithms used in Fig. 1. The kinematic model of a sample five-axis machine tool is modeled with the screw theory in Section 2. The concept of error twists is introduced to build a 3D volumetric error map of the machine in Section 3. Section 4 presents a methodology to identify all the errors of rotary axes, and Section 5 demonstrates the compensation strategy of volumetric errors. The paper is concluded in Section 6 by summarizing the effectiveness of the method and its practical application in CNC systems.

2. Kinematic model of five-axis machine tools

Although any serial, five-axis kinematic configuration can be modeled with the generalized kinematic model developed in our Virtual CNC [3], a machine tool with 3 translational and a trunnion with 2 rotary drives is used to illustrate the proposed modeling of volumetric errors and their compensation (Fig. 2). The MCS is

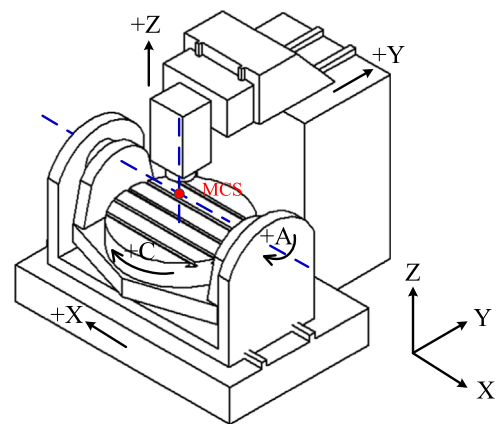


Fig. 2. Configuration of the five-axis machine tool.

defined at the intersection of the centerlines of the two rotary axes. The objective is to predict the relative error between the tool tip and workpiece clamped on the table as the drives move within the workspace of the machine. The kinematics of the machine is modeled using screw theory as presented in [3] and summarized for the particular five-axis machine used here.

The motion commands to the five drives ($x, y, z, \theta_A, \theta_C$) are used to predict the position and orientation of the tool tip relative to the

workpiece (X, Y, Z, I, J, K) using the forward kinematics of the machine (see CAM section in Fig. 1).

The five-axis machine tool is represented by the workpiece and the tool chains. If the individual drives of the machine move ($x, y, z, \theta_A, \theta_C$) amount, the new coordinates of the workpiece and the tool tip in MCS can be evaluated using screw motions ($e^{\hat{\xi}\cdot\theta}$) with twists (ξ) as:

$$\left. \begin{aligned} g_{bw} &= e^{\hat{\xi}_X \cdot (-x)} \cdot e^{\hat{\xi}_A \cdot (-\theta_A)} \cdot e^{\hat{\xi}_C \cdot (-\theta_C)} \cdot g_{bw}(0) \dots \\ g_{bt} &= e^{\hat{\xi}_Y \cdot y} \cdot e^{\hat{\xi}_Z \cdot z} \cdot g_{bt}(0) \end{aligned} \right\} \quad (1)$$

where, $g_{bw}(0)$ and $g_{bt}(0)$ are the initial 4×4 motion matrices of the workpiece and the tool tip relative to the MCS. The transformation matrix from the tool tip to the workpiece can be obtained from Eq. (1) as:

$$\begin{aligned} g_{wt} &= g_{wb} \cdot g_{bt} = (g_{bw})^{-1} \cdot g_{bt} \\ &= g_{bw}^{-1}(0) \cdot e^{\hat{\xi}_C \cdot \theta_C} \cdot e^{\hat{\xi}_A \cdot \theta_A} \cdot e^{\hat{\xi}_X \cdot x} \cdot e^{\hat{\xi}_Y \cdot y} \cdot e^{\hat{\xi}_Z \cdot z} \cdot g_{bt}(0) \end{aligned} \quad (2)$$

The twist for a rotary axis is expressed as:

$$\xi = \begin{bmatrix} \mathbf{v} \\ \boldsymbol{\omega} \end{bmatrix}, \mathbf{v} = \mathbf{q} \times \boldsymbol{\omega} \quad (3)$$

where, $\boldsymbol{\omega}$ is the unit vector in the positive direction of the rotary axis-line and \mathbf{q} is any point on the axis-line expressed in MCS, i.e., for A-axis, $\boldsymbol{\omega} = [1 \ 0 \ 0]^T$, $\mathbf{q} = [x \ 0 \ 0]^T$. The screw motion of the rotary axes has the form [22]:

$$e^{\hat{\xi}\cdot\theta} = \begin{bmatrix} e^{\hat{\omega}\theta} & (\mathbf{I}_{3 \times 3} - e^{\hat{\omega}\theta})(\boldsymbol{\omega} \times \mathbf{v}) + \boldsymbol{\omega}\boldsymbol{\omega}^T \mathbf{v}\theta \\ \mathbf{0}_{1 \times 3} & 1 \end{bmatrix} \quad (4)$$

where θ is the angular rotation of the axis. For the A-axis, the $e^{\hat{\omega}\theta}$ can be expanded as:

$$\begin{aligned} e^{\hat{\omega}\theta} &= \mathbf{I}_{3 \times 3} + \hat{\boldsymbol{\omega}} \cdot \sin \theta + \hat{\boldsymbol{\omega}}^2 \cdot (1 - \cos \theta) \\ &= \mathbf{I}_{3 \times 3} + \begin{bmatrix} 0 & 0 & 0 \\ 0 & 0 & -1 \\ 0 & 1 & 0 \end{bmatrix} \cdot \sin \theta_A + \begin{bmatrix} 0 & 0 & 0 \\ 0 & 0 & -1 \\ 0 & 1 & 0 \end{bmatrix}^2 \cdot (1 - \cos \theta_A) \end{aligned} \quad (5)$$

The $\hat{\cdot}$ operator converts vector to matrix as $\hat{\mathbf{a}}\mathbf{b} = \mathbf{a} \times \mathbf{b}$. The screw motion for translational axes is expressed as:

$$\xi = \begin{bmatrix} \mathbf{v} \\ \mathbf{0} \end{bmatrix}, e^{\hat{\xi}\cdot\theta} = \begin{bmatrix} \mathbf{I}_{3 \times 3} & \mathbf{v}\cdot\theta \\ \mathbf{0}_{1 \times 3} & 1 \end{bmatrix} \quad (6)$$

where, \mathbf{v} is the unit vector of the positive direction, i.e., for X-axis, $\mathbf{v} = [1 \ 0 \ 0]^T$. The detailed derivation of the screw motion can be found in References [3,22].

Compared with the traditional HTM method, the screw theory-based modeling has 2 advantages: the motions are defined in the MCS, and therefore no local coordinate system is needed; it provides explicit mathematical solutions to the inverse kinematics.

3. Modeling of volumetric errors

The volumetric errors of the machine are modeled by introducing 1 error twist for each component error of the drive. The error twists are then mapped to the machine's working space and drives with the aid of the kinematic model of the five-axis machine as follows.

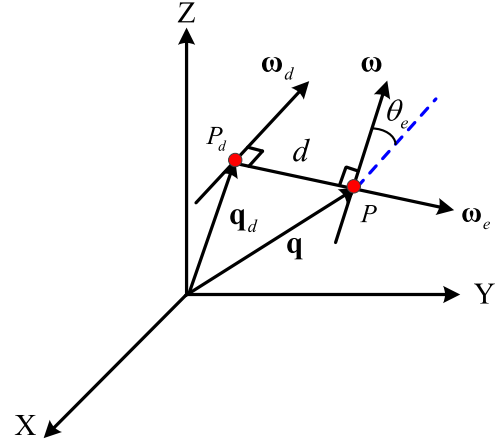


Fig. 3. Error twist.

3.1. Error twists (ξ_e)

Error twists are used to model the geometric errors between the tool tip and the workpiece. Assume that the ideal position of the machine is at P_d , and the ideal direction of the linear axis or rotation axis of the rotary drive is $\boldsymbol{\omega}_d$ (Fig. 3). However, the real machine position, perhaps at P and the axis may have an angular error of θ_e . The ideal twist ξ_d and the actual twist ξ with geometric errors can be expressed as:

$$\xi_d = [\mathbf{q}_d \times \boldsymbol{\omega}_d \quad \boldsymbol{\omega}_d]^T, \xi = [\mathbf{q} \times \boldsymbol{\omega} \quad \boldsymbol{\omega}]^T \quad (7)$$

The change from the ideal twist ξ_d to the actual twist ξ can be regarded as the result of an error motion $e^{\hat{\xi}_e \cdot \theta_e}$. The error twist ξ_e consists of an angular geometric error θ_e around the common perpendicular line of the ideal and the actual axis lines, and the linear position error d of the axis. The error twist $\xi_e = [\mathbf{v}_e \quad \boldsymbol{\omega}_e]^T$ can be expressed as:

$$\left. \begin{aligned} \boldsymbol{\omega}_e &= \frac{\boldsymbol{\omega}_d \times \boldsymbol{\omega}}{\sin \theta_e}, h_e = \frac{d}{\theta_e} = \frac{|\mathbf{q} - \mathbf{q}_d|}{\theta_e} \\ \mathbf{v}_e &= \frac{\mathbf{q} \times (\boldsymbol{\omega}_d \times \boldsymbol{\omega})}{\sin \theta_e} + h_e \frac{\boldsymbol{\omega}_d \times \boldsymbol{\omega}}{\sin \theta_e} = \frac{\mathbf{q}_d \times \mathbf{q}}{d} + \frac{\mathbf{q} - \mathbf{q}_d}{\theta_e} \end{aligned} \right\} \quad (8)$$

When the angular geometric error is zero ($\theta_e = 0$), the actual axial-line is parallel to the ideal axis-line, and thus the twist vector contains only translational errors ($\boldsymbol{\omega}_e = 0, h_e = \infty$) and the error twist changes to:

$$\xi_e = \begin{bmatrix} \frac{\mathbf{q} - \mathbf{q}_d}{d} \\ \mathbf{0} \end{bmatrix} \quad (9)$$

When $d = 0$, i.e. $h_e = 0, \mathbf{q} = \mathbf{q}_d$, the actual and ideal axes coincide without linear errors, and hence the error twist indicates only angular errors:

$$\xi_e = \begin{bmatrix} \mathbf{v}_e \\ \boldsymbol{\omega}_e \end{bmatrix} = \begin{bmatrix} \mathbf{q} \times (\boldsymbol{\omega}_d \times \boldsymbol{\omega}) & \boldsymbol{\omega}_d \times \boldsymbol{\omega} \\ \sin \theta_e & \sin \theta_e \end{bmatrix}^T \quad (10)$$

As an example, let's assume that the rotary drive C has a tilt error (ϵ_{yc}) around the Y-axis. The coordinate system of the C drive is defined in MCS as $\mathbf{q} = [0_x \ 0_y \ 0_z]^T$ (see Fig. 3 and Fig. 4).

Based on Eq. (8), $\boldsymbol{\omega}_e$ and \mathbf{v}_e can be expressed as:

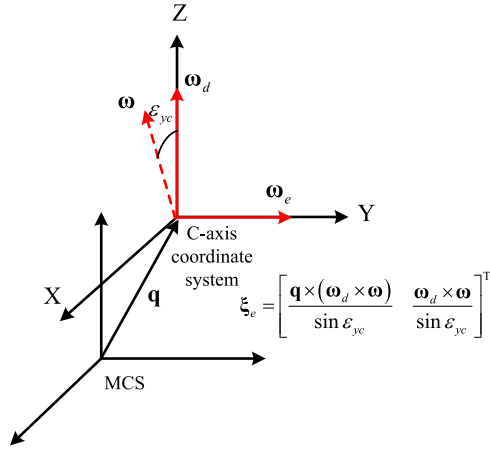


Fig. 4. Example of error twist.

Table 1
41 geometric errors of the AC table tilting five-axis machine tool.

X-axis	Y-axis	Z-axis	Squareness error	A-axis	C-axis	PIGEs of Rotary axes
δ_{xx}	δ_{yy}	δ_{zz}	S_{xy}	δ_{xa}	δ_{xc}	δ_{xoc} S_{boa}
δ_{yx}	δ_{xy}	δ_{xz}	S_{yz}	δ_{ya}	δ_{yc}	δ_{yoc} S_{coa}
δ_{zx}	δ_{zy}	δ_{yz}	S_{xz}	δ_{za}	δ_{zc}	δ_{zoc} S_{coa}
ϵ_{xx}	ϵ_{xy}	ϵ_{xz}		ϵ_{xa}	ϵ_{xc}	δ_{zoc} S_{boc}
ϵ_{yx}	ϵ_{yy}	ϵ_{yz}		ϵ_{ya}	ϵ_{yc}	(ISO 230-7)
ϵ_{zx}	ϵ_{zy}	ϵ_{zz}		ϵ_{za}	ϵ_{zc}	

$$\begin{cases} \omega_e = [0 \ 1 \ 0]^T \\ \mathbf{v}_e = \mathbf{q} \times \omega_e = \begin{bmatrix} 0_x \\ 0_y \\ 0_z \end{bmatrix} \times \begin{bmatrix} 0 \\ 1 \\ 0 \end{bmatrix} \end{cases} \quad (11)$$

which leads to the error twist $\xi_e = [\mathbf{v}_e \ \omega_e]^T$. The geometric errors of all axes can be defined in a similar fashion.

3.2. Modeling of volumetric errors with error twists

Table 1 lists 41 geometric errors of the five-axis machine tool. Each axis has 6 position-dependent geometric errors (PDGEs). A linear axis has 1 positioning, 2 straightness and 3 angular (roll, pitch and yaw) errors as shown in Fig. 5. For example, the errors for the linear X-axis are δ_{xx} , $(\delta_{yx}, \delta_{zx})$, $(\epsilon_{xx}, \epsilon_{yx}, \epsilon_{zx})$. A rotary axis has 1 axial error indicating the linear offset of the axis of rotation,

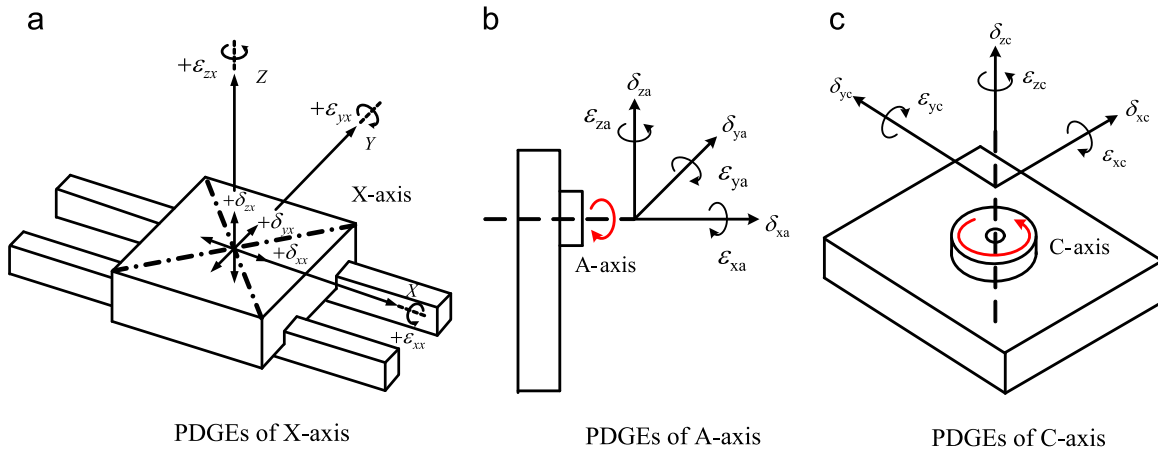


Fig. 5. Definitions of PDGEs.

2 radial errors, 1 angular positioning error and 2 tilt errors, i.e., the errors of rotary drive C are δ_{zc} , $(\delta_{xc}, \delta_{yc})$, ϵ_{zc} , and $(\epsilon_{xc}, \epsilon_{yc})$. In addition, 3 PIGEs, the squareness errors (S_{xy} , S_{yz} , S_{xz}), lie between the 3 linear axes (X, Y, Z), and 8 PIGEs (δ_{xoc} , δ_{yoc} , δ_{yoc} , δ_{zoc} , S_{boa} , S_{boc} , S_{boa} , S_{coa}) lie between the 2 rotary axes [23] (see Fig. 6).

Parameters $e^{\hat{\xi}_{ei}^I \theta_{ei}^I}$ and $e^{\hat{\xi}_{ei}^D \theta_{ei}^D}$ represent the PIGE and PDGE matrices of the axis i ($i=X, Y, Z, A, C$), respectively.

The PDGE matrix of the axis i can be evaluated by the products of its 6 error motions as

$$\begin{aligned} e^{\hat{\xi}_{ei}^D \theta_{ei}^D} &= T(\delta_{xi})T(\delta_{yi})T(\delta_{zi})R(\epsilon_{xi})R(\epsilon_{yi})R(\epsilon_{zi}) \\ &= e^{\hat{\xi}_{\delta_{xi}} \delta_{xi}} \cdot e^{\hat{\xi}_{\delta_{yi}} \delta_{yi}} \cdot e^{\hat{\xi}_{\delta_{zi}} \delta_{zi}} \cdot e^{\hat{\xi}_{\epsilon_{xi}} \epsilon_{xi}} \cdot e^{\hat{\xi}_{\epsilon_{yi}} \epsilon_{yi}} \cdot e^{\hat{\xi}_{\epsilon_{zi}} \epsilon_{zi}} \end{aligned} \quad (12)$$

The modeling of PIGEs is however detailed as follows:

3.3. Squareness errors of the translational axes

For the five-axis machine tool with a configuration shown in Figs. 2, 3 squareness errors of linear axes are illustrated in Fig. 6. When measuring the squareness errors, the X-axis is set as the reference, and the squareness error is positive when the angle between 2 axes is greater than 90 degrees.

The PIGE models of translational axes are obtained from the error twists as follows:

$$\begin{cases} e^{\hat{\xi}_{eY}^I \theta_{eY}^I} = e^{\hat{\xi}_{eS_{xy}} S_{xy}} \\ e^{\hat{\xi}_{eZ}^I \theta_{eZ}^I} = e^{\hat{\xi}_{eS_{yz}} S_{yz}} \cdot e^{\hat{\xi}_{eS_{xz}} (-S_{xz})} \end{cases} \quad (13)$$

3.4. Modeling of 8 PIGEs of rotary axes

ISO 230-7 defines 8 PIGEs of 2 rotary axes, which are displayed in Fig. 6. Similar to the modeling of squareness errors, the PIGE models of the A- and C-axis are expressed as:

$$\begin{cases} e^{\hat{\xi}_{eC}^I \theta_{eC}^I} = e^{\hat{\xi}_{\delta_{xoc}} \delta_{xoc}} \cdot e^{\hat{\xi}_{\delta_{yoc}} \delta_{yoc}} \cdot e^{\hat{\xi}_{\delta_{zoc}} \delta_{zoc}} \cdot e^{\hat{\xi}_{S_{aoc}} S_{aoc}} \cdot e^{\hat{\xi}_{S_{boc}} (-S_{boc})} \\ e^{\hat{\xi}_{eA}^I \theta_{eA}^I} = e^{\hat{\xi}_{\delta_{yoc}} \delta_{yoc}} \cdot e^{\hat{\xi}_{\delta_{zoc}} \delta_{zoc}} \cdot e^{\hat{\xi}_{S_{boa}} S_{boa}} \cdot e^{\hat{\xi}_{S_{coa}} (-S_{coa})} \end{cases} \quad (14)$$

After adding all the error motion matrices into Eq. (1), the final forward kinematics model of the five-axis machine tool can be obtained as:

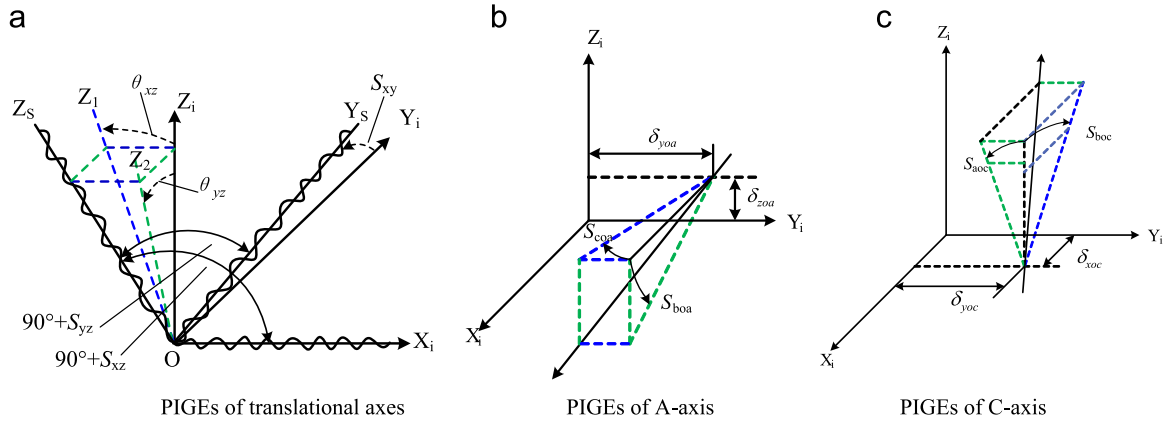


Fig. 6. Definitions of PIGEs.

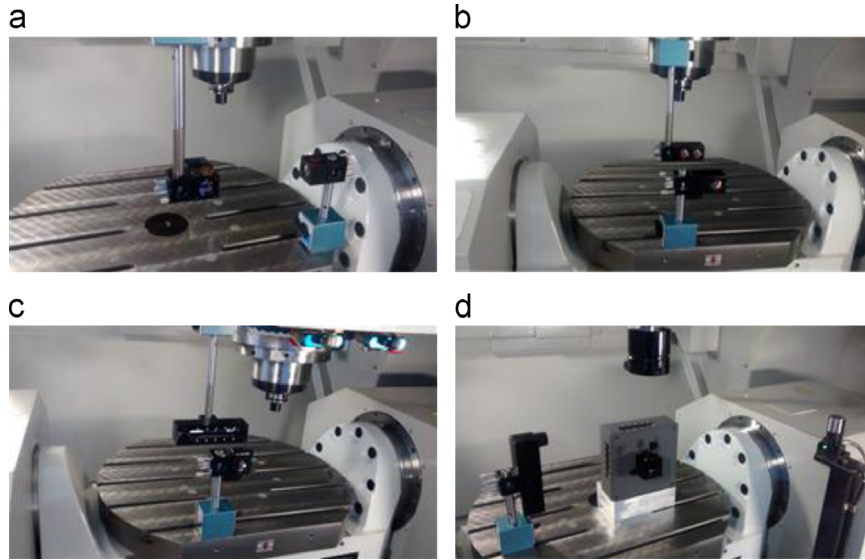


Fig. 7. Measurements set-ups of laser interferometer. (a) Positioning error, (b) Angular error, (c) Straightness error, (d) Squareness error.

$$\left. \begin{aligned}
 g_{bw}^e &= \left(e^{\hat{\xi}^I X \cdot (-x)}, e^{\hat{\xi}^D e^X \cdot \theta e^X} \right) \cdot \left(e^{\hat{\xi}^I e^A \cdot \theta e^A}, e^{\hat{\xi}^D e^A \cdot \theta e^A}, e^{\hat{\xi}^I A \cdot (-\theta A)} \right) \\
 &\quad \cdot \left(e^{\hat{\xi}^I e^C \cdot \theta e^C}, e^{\hat{\xi}^D e^C \cdot \theta e^C}, e^{\hat{\xi}^I C \cdot (-\theta C)} \right) \cdot g_{bw}(0) \\
 g_{bt}^e &= \left(e^{\hat{\xi}^I e^Y \cdot \theta e^Y}, e^{\hat{\xi}^D e^Y \cdot \theta e^Y}, e^{\hat{\xi}^I e^Z \cdot \theta e^Z} \right) \cdot \left(e^{\hat{\xi}^I e^Z \cdot \theta e^Z}, e^{\hat{\xi}^D e^Z \cdot \theta e^Z}, e^{\hat{\xi}^I e^Z \cdot \theta e^Z} \right) \cdot g_{bt}(0)
 \end{aligned} \right\} \quad (15)$$

$$g_{wt}^e = g_{wb}^e \cdot g_{bt}^e = (g_{bw}^e)^{-1} \cdot g_{bt}^e \quad (16)$$

4. Geometric errors identification and measurement

All the 21 geometric errors of linear axes except for 3 roll errors have been measured by a laser interferometer. The measurement set-ups for the positioning, angular, straightness and squareness errors of linear axes are shown in Fig. 7. A ballbar is used to measure 1 axial, 2 radial, 1 angular positioning and 2 tilt errors, as well 4 PIGEs per rotary axis.

4.1. Measuring patterns for PIGEs and PDGEs of rotary axes

It is noted that the PIGEs of the rotary axes shown in Fig. 6 are defined in the MCS of the five-axis machine tool shown in Fig. 2.

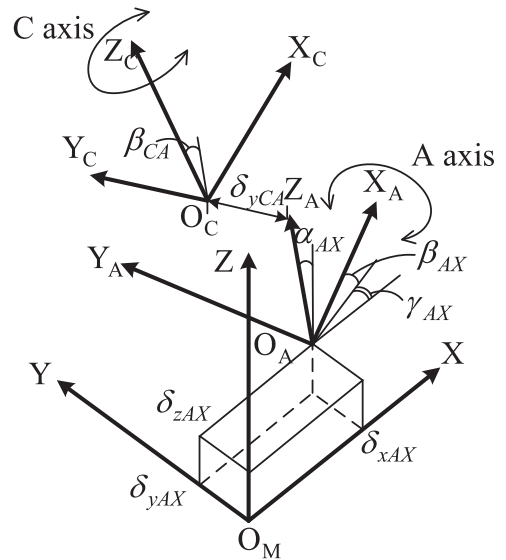


Fig. 8. Definition of PIGEs of AC rotary axes (relative notation).

For five-axis machines with table or spindle tilting [24] configurations, these error parameters (Eq.(14)) are not suitable for kinematic modeling because the PIGEs of the “higher” rotary axis are

influenced by the motion of the “lower” rotary axis. For example, assume the C-axis has a tilting error around the Y-axis of the MCS at A=0. However, this error tilts the C-axis around the Z-axis of the MCS at A=-90. Therefore, for the five-axis machine tool depicted in Fig. 2, the relative notation suggested by Ibaraki [11,12,14] is to be used here instead of the absolute notation proposed in ISO 230-7 standards. These two notations can convert to each other [8]. Eight PIGEs of relative notations are illustrated in Figs. 8, and 12 PDGEs are presented in Fig. 5.

The patterns shown in Fig. 9 are used for ballbar tests as suggested by Tsutsumi [25,26]. H indicates the vertical distance between the table-side ball and the center-line of the A-axis (Fig. 9a-c), while L represents the horizontal distance between the table-side ball and the center-line of the C-axis (Fig. 9d-f). Before running the ballbar tests, the backlash of the linear axes is measured and compensated by the CNC controller.

The kinematic model of the table-side ball can be expressed based on error twists as:

$$\begin{aligned} \begin{bmatrix} x_T \\ y_T \\ z_T \\ 1 \end{bmatrix} &= PIGE_A \cdot PDGE_A \cdot T_{A-ideal} \cdot PIGE_C \cdot PDGE_C \cdot T_{C-ideal} \cdot \begin{bmatrix} L \\ 0 \\ H \\ 1 \end{bmatrix} = e^{\hat{\xi}_{eA}^I \cdot \theta_{eA}^I} \cdot e^{\hat{\xi}_{eA}^D \cdot \theta_{eA}^D} \cdot e^{\hat{\xi}_{eA}(-\theta_A)} \cdot e^{\hat{\xi}_{eC}^I \cdot \theta_{eC}^I} \cdot e^{\hat{\xi}_{eC}^D \cdot \theta_{eC}^D} \cdot e^{\hat{\xi}_{eC}(-\theta_C)} \cdot \begin{bmatrix} L \\ 0 \\ H \\ 1 \end{bmatrix} \\ &= \underbrace{\begin{bmatrix} 1 & 0 & 0 & \delta_{xAX} \\ 0 & 1 & 0 & \delta_{yAX} \\ 0 & 0 & 1 & \delta_{zAX} \\ 0 & 0 & 0 & 1 \end{bmatrix}}_{PIGE_A} \cdot \underbrace{\begin{bmatrix} 1 & -\gamma_{AY} & \beta_{AY} & 0 \\ \gamma_{AY} & 1 & 0 & 0 \\ -\beta_{AY} & 0 & 1 & 0 \\ 0 & 0 & 0 & 1 \end{bmatrix}}_{PDGE_A} \cdot \underbrace{\begin{bmatrix} 1 & -\varepsilon_{za} & \varepsilon_{ya} & \delta_{xa} \\ \varepsilon_{za} & 1 & -\varepsilon_{xa} & \delta_{ya} \\ -\varepsilon_{ya} & \varepsilon_{xa} & 1 & \delta_{za} \\ 0 & 0 & 0 & 1 \end{bmatrix}}_{T_{A-ideal}} \cdot \underbrace{\begin{bmatrix} 1 & 0 & 0 & 0 \\ 0 & \cos(-a + \alpha_{AY}) & -\sin(-a + \alpha_{AY}) & 0 \\ 0 & \sin(-a + \alpha_{AY}) & \cos(-a + \alpha_{AY}) & 0 \\ 0 & 0 & 0 & 1 \end{bmatrix}}_{T_{A-ideal}} \\ &= \underbrace{\begin{bmatrix} 1 & 0 & 0 & 0 \\ 0 & 1 & 0 & \delta_{yCA} \\ 0 & 0 & 1 & 0 \\ 0 & 0 & 0 & 1 \end{bmatrix}}_{PIGE_C} \cdot \underbrace{\begin{bmatrix} 1 & 0 & \beta_{CA} & 0 \\ 0 & 1 & 0 & 0 \\ -\beta_{CA} & 0 & 1 & 0 \\ 0 & 0 & 0 & 1 \end{bmatrix}}_{PDGE_C} \cdot \underbrace{\begin{bmatrix} 1 & -\varepsilon_{zc} & \varepsilon_{yc} & \delta_{xc} \\ \varepsilon_{zc} & 1 & -\varepsilon_{xc} & \delta_{yc} \\ -\varepsilon_{yc} & \varepsilon_{xc} & 1 & \delta_{zc} \\ 0 & 0 & 0 & 1 \end{bmatrix}}_{T_{C-ideal}} \cdot \underbrace{\begin{bmatrix} \cos(-c) & -\sin(-c) & 0 & 0 \\ \sin(-c) & \cos(-c) & 0 & 0 \\ 0 & 0 & 1 & 0 \\ 0 & 0 & 0 & 1 \end{bmatrix}}_{T_{C-ideal}} \cdot \begin{bmatrix} L \\ 0 \\ H \\ 1 \end{bmatrix} \end{aligned} \quad (17)$$

When the A-axis is active and the C-axis is stationary (Fig. 9.a-c), the matrices $PDGE_C$ and $T_{C-ideal}$ become unit matrices. Similarly, when the C-axis is active and the A-axis is stationary (Fig. 9d-f), the matrices $PDGE_A$ and $T_{A-ideal}$ become unit matrices. However, the PIGEs of A- and C-axis will always influence the table-side ball even when the angle of the A- or C-axis is constant.

4.2. Decoupling method of PIGEs and PDGEs

Here the A-axis is given as an example to demonstrate the decoupling method of PIGEs and PDGEs. From Eq.(17), the deviations in the X, Y and Z directions can be evaluated as:

$$\begin{cases} \Delta_x = \delta_{xa} + H \cdot \varepsilon_{ya} \cdot \cos(-a) + H \cdot \varepsilon_{za} \cdot \sin(-a) + f_{PIGE-x} \\ \Delta_y = \delta_{ya} + L \cdot \varepsilon_{za} - H \cdot \varepsilon_{xa} \cdot \cos(-a) + f_{PIGE-y} \\ \Delta_z = \delta_{za} - L \cdot \varepsilon_{ya} - H \cdot \varepsilon_{xa} \cdot \sin(-a) + f_{PIGE-z} \end{cases} \quad (18)$$

where, the deviations caused by PIGEs (f_{PIGE}) are expressed as:

$$\begin{cases} f_{PIGE-x} = \delta_{xAX} + H \cdot \beta_{CA} + H \cdot \cos(-a) \cdot \beta_{AX} + H \cdot \sin(-a) \cdot \gamma_{AX} \\ f_{PIGE-y} = \delta_{yAX} + L \cdot \gamma_{AX} + \delta_{yCA} \cdot \cos(-a) - H \cdot \cos(-a) \\ \quad \cdot \alpha_{AX} + L \cdot \sin(-a) \cdot \beta_{CA} \\ f_{PIGE-z} = \delta_{zAX} - L \cdot \beta_{AX} + \delta_{yCA} \cdot \sin(-a) - L \cdot \cos(-a) \\ \quad \cdot \beta_{CA} - H \cdot \sin(-a) \cdot \alpha_{AX} \end{cases} \quad (19)$$

Fig. 10 shows the sensitive directions of the ballbar, and gives error decompositions in radial, tangential and axial patterns of the A-axis.

Step 1 Calibration of PIGEs: First assume the PDGEs do not exist and the 8 PIGEs can be obtained by reading the eccentricities measured by the ballbar as [9]:

Radial direction of the A axis:

$$\begin{cases} e_{yRA} = -\delta_{yAX} \\ e_{zRA} = -\delta_{zAX} \end{cases} \quad (20)$$

Axial direction of the A axis:

$$\begin{cases} e_{yAA} = H \cdot \gamma_{AX} \\ e_{zAA} = -H \cdot \beta_{AX} \end{cases} \quad (21)$$

Radial direction of the C axis:

$$\begin{cases} e_{xRC} = -\delta_{xAX} - H \cdot \beta_{CA} - H \cdot \beta_{AX} \\ e_{yRC} = -\delta_{yAX} - \delta_{yCA} + H \cdot \alpha_{AX} \end{cases} \quad (22)$$

Axial direction of the C axis:

$$\begin{cases} e_{xAC} = L \cdot \beta_{CA} + L \cdot \beta_{AX} \\ e_{yAC} = -L \cdot \alpha_{AX} \end{cases} \quad (23)$$

Step 2 Calibration of PDGEs: However, the PIGEs always exist with PDGEs, and they affect the ballbar readings together. The ballbar readings in axial (ρ_a), radial (ρ_r) and tangential (ρ_t) directions are shown as follows.

Axial direction of the A axis:

$$\rho_a = \Delta x \quad (24)$$

— Path of table side ball — Path of spindle side ball

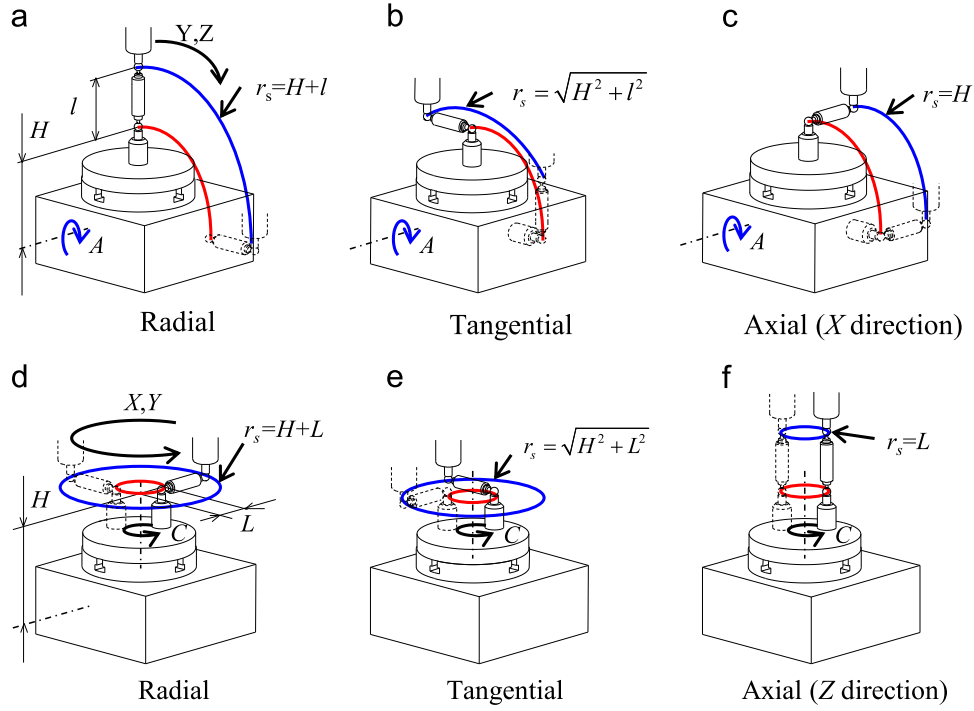


Fig. 9. Measuring patterns for A- and C-axis [26].

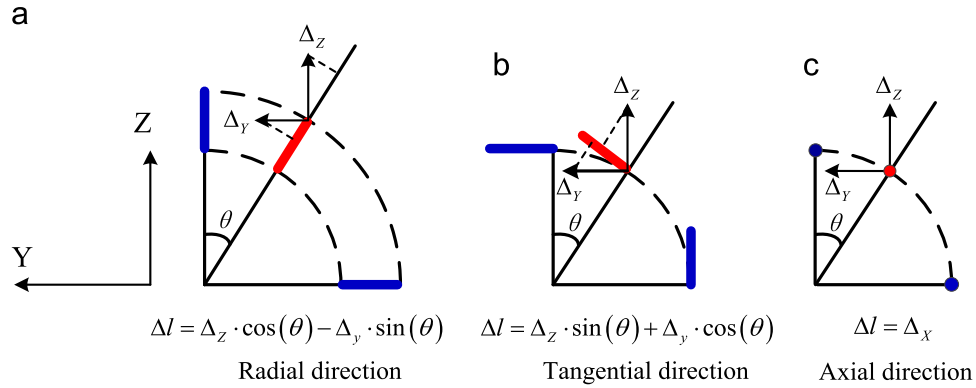


Fig. 10. Sensitive directions of the ballbar and error decompositions.

Table 2
Eight PIGEs evaluated by the proposed simultaneous and Tsutsumi's [9] methods.

Type	α_{AX}	β_{AX}	γ_{AX}	β_{CA}	δ_{xAX}	δ_{yAX}	δ_{zAX}	δ_{yCA}
Separately calculated [9]	-10.3°	-57.5°	-46.0°	78.1°	53 μm	25 μm	-20 μm	12.6 μm
Simultaneously Calculated	6.3°	-37.5°	-31.5°	48.7°	46 μm	21 μm	-12 μm	20.5 μm

Radial direction of the A axis:

$$\rho_r = \Delta z \cdot \cos(-a) - \Delta y \cdot \sin(-a)$$

Tangential direction of the A-axis:

$$\rho_t = \Delta z \cdot \sin(-a) + \Delta y \cdot \cos(-a) \quad (26)$$

The influence of PIGEs can be extracted by substituting the PIGEs obtained in Step 1 as:

$$\begin{cases} \rho'_a = \rho_a - f_{PIGE-x} \\ \rho'_r = \rho_r - [f_{PIGE-z} \cdot \cos(-a) - f_{PIGE-y} \cdot \sin(-a)] \\ \rho'_t = \rho_t - [f_{PIGE-z} \cdot \sin(-a) + f_{PIGE-y} \cdot \cos(-a)] \end{cases} \quad (27)$$

By substituting Eq. (19) into Eq. (27), the axial, radial and tangential errors can be listed as:

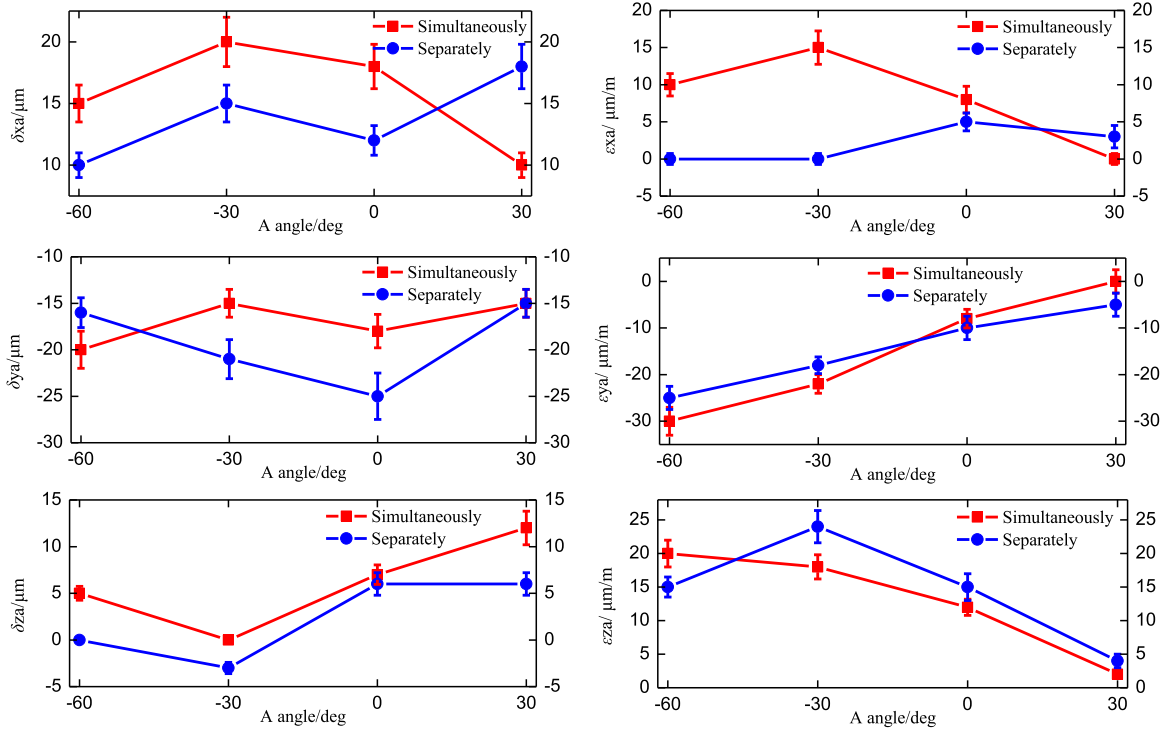


Fig. 11. PDGEs of A-axis defined by two different methods.

$$\begin{cases}
 \rho'_a = \delta_{xa} + H \cdot \epsilon_{ya} \cdot \cos(-a) + H \cdot \epsilon_{za} \cdot \sin(-a) \\
 \rho'_r = \delta_{za} \cdot \cos(-a) - \delta_{ya} \cdot \sin(-a) - L \cdot \epsilon_{ya} \cdot \cos(-a) - L \cdot \epsilon_{za} \\
 \quad \cdot \sin(-a) \\
 \rho'_t = \delta_{za} \cdot \sin(-a) + \delta_{ya} \cdot \cos(-a) - H \cdot \epsilon_{xa} - L \cdot \epsilon_{ya} \cdot \\
 \quad \sin(-a) + L \cdot \epsilon_{za} \cdot \cos(-a)
 \end{cases} \quad (28)$$

Three tests with different values of H and L ($(H, 0)$, $(H_1, 0)$, (H, L)) are conducted to calibrate the 6 PDGEs of the A-axis [19]. The 3 groups of ballbar readings are recorded: $(\rho_{a1}, \rho_{r1}, \rho_{t1})$, $(\rho_{a2}, \rho_{r2}, \rho_{t2})$ and $(\rho_{a3}, \rho_{r3}, \rho_{t3})$. Substituting these ballbar readings into Eqs. (27), (28), the final results of 6 PDGEs are obtained as:

$$\begin{cases}
 \delta_{za} = \frac{H[\rho'_{r2} \cdot \cos(-a) + \rho'_{t2} \cdot \sin(-a)] + (H_1 - 2H)[\rho'_{r1} \cdot \cos(-a) + \rho'_{t1} \cdot \sin(-a)]}{H_1 - H} \\
 \epsilon_{xa} = \frac{(\rho'_{r2} - \rho'_{r1}) \cdot \cos(-a) + (\rho'_{t2} - \rho'_{t1}) \cdot \sin(-a)}{(H_1 - H) \cdot \sin(-a)} \\
 \delta_{ya} = \frac{\delta_{za} \cdot \cos(-a) - \rho'_{r1}}{\sin(-a)} \\
 \epsilon_{za} = \frac{\cos(-a) \cdot (\rho'_{t3} + H \cdot \epsilon_{xa}) - \sin(-a) \cdot \rho'_{r3} - \delta_{ya}}{L} \\
 \epsilon_{ya} = -\frac{\rho'_{r3} - \delta_{za} \cdot \cos(-a) + \delta_{ya} \cdot \sin(-a) + L \cdot \epsilon_{za} \cdot \sin(-a)}{L \cdot \cos(-a)} \\
 \delta_{xa} = \rho'_{a1} - H \epsilon_{ya} \cos(-a) - H \epsilon_{za} \sin(-a)
 \end{cases} \quad (29)$$

Step 3 Iteration: Substituting the PDGEs back into Eq. (18), the revised PIGEs can be obtained, which are then used to recalculate PDGEs. After iteration, the values of PIGEs and PDGEs are obtained.

Similarly, the PDGEs and PIGEs of the C-axis can be obtained with the same 3 steps with the patterns described in Fig. 9. In addition, this decoupling method can also be applied to the orthogonal measuring patterns proposed in Ref. [26].

4.3. Experimental results

After compensating the positioning errors of 3 translational axes with the CNC, ballbar tests are conducted using the measuring patterns shown in Fig. 9. PIGEs and PDGEs are decoupled simultaneously. PIGEs results calculated separately by the Tsutsumi's method [9] are compared against the proposed decoupling method in Table 2. The set-up errors of the ballbar can be analyzed using the method presented in Refs. [27, 28].

PDGEs of the A- and C-axis defined by the proposed simultaneous method are compared with Zhu's [19] separate measurement method in Fig. 11 and Fig. 12, respectively. Zhu models PDGEs without considering PIGEs. The differences between the results of these 2 methods mainly come from the mutual influences between the PIGEs and PDGEs. As shown in Eq. (27), when decoupling the PDGEs, the influence of the PIGEs should be removed and vice versa. Usually the PDGEs are relatively smaller than PIGEs, and therefore, the mutual influence between them may have little influence on decoupling the PIGEs but a large influence on PDGEs. Simultaneously decoupling these 2 groups of errors can obtain more accurate results than decoupling them separately.

5. Compensation of volumetric errors

The proposed flowchart of the volumetric compensation algorithm for five-axis machine tools is shown in Fig. 1.

NC part programs are generated by a Computer Aided Manufacturing (CAM) system, and the tool tip position and tool axis orientation vector ($\mathbf{P} = [X \ Y \ Z \ I \ J \ K]^T$), i.e., the Cutter Location (CL) file, are represented in PCS. A postprocessor transforms the motions to drive commands (G-codes) in PCS using the inverse kinematics model of the machine (Step 1). The CNC considers the jerk, acceleration and velocity profiles and generates drive commands $(x, y, z, \theta_A, \theta_C)$ at discrete time intervals (i.e., $T=1$ ms) [29]. However, the real tool position becomes $\mathbf{P}' = [X' \ Y' \ Z' \ I' \ J' \ K']^T$ due to geometric errors of the machine which can be predicted by

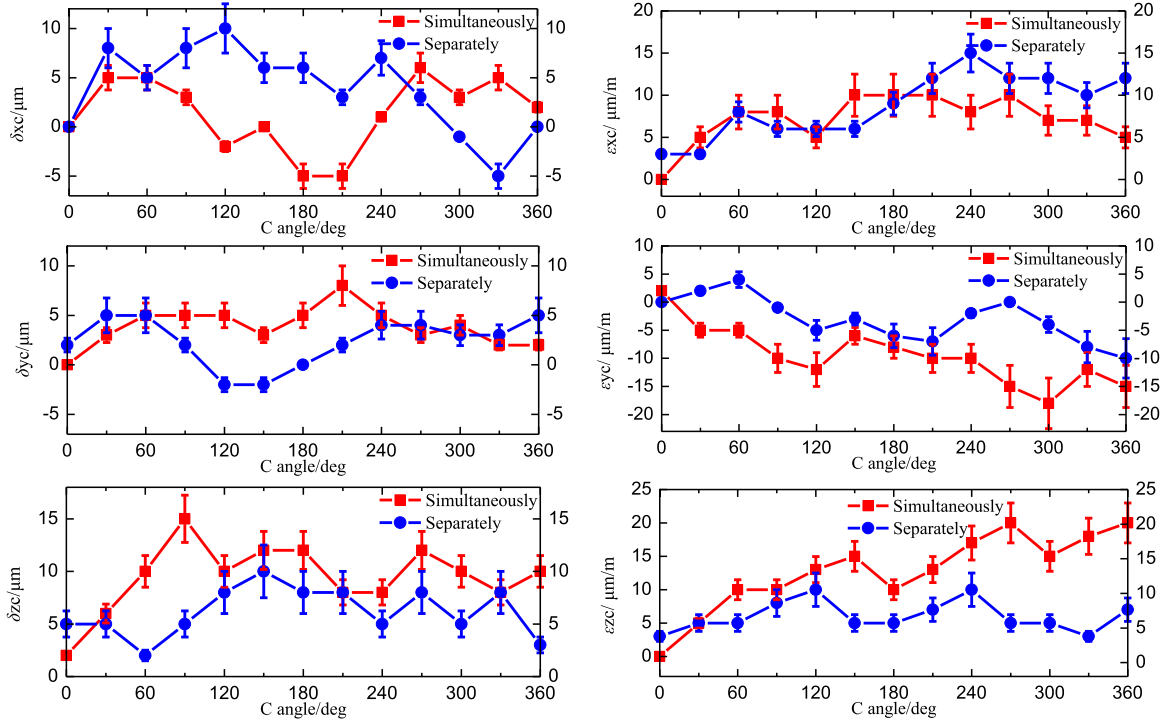


Fig. 12. PDGEs of C-axis defined by two different methods.

the forward kinematics of the machine with the volumetric error model (Eq. (16)) (Steps 2, 4, and 5 as presented in Section 3). The predicted tool position and orientation with geometric errors (P') are compared against the ideal desired trajectory (P) to predict the error components (Step 6) as:

$$\Delta = [X - X' \ Y - Y' \ Z - Z' \ I - I' \ J - J' \ K - K']^T \quad (30)$$

If the translational ($\Delta x, \Delta y, \Delta z$) and orientation ($\Delta I, \Delta J, \Delta K$) errors are larger than the set tolerances, they are added to the desired trajectory (P) (Step 7) as:

$$P_c = [P + \Delta] \quad (31)$$

where P_c is the new tool position command vector with geometric error compensation. P_c is passed through the inverse kinematics of the machine to generate drive commands with geometric error compensation components ($x_c, y_c, z_c, \theta_{A_c}, \theta_{C_c}$) (Step 8).

However, this linear method does not compensate all the errors because of the nonlinear kinematics of five-axis machine tools. If the volumetric errors are large, the residual errors could still be out of tolerance, and a second iteration may be needed when the machine errors are large.

The compensation of geometric errors is carried out by mapping the measured errors from MCS to PCS where the actual compensation is made (Step 5), and the evaluation of inverse kinematics is done (Step 8).

5.1. Mapping of geometric errors from MCS to PCS

The MCS is set in the CNC by the manufacturer where the axis errors are measured, and the PCS is set at a convenient location on the part by the NC programmer. Since the error measurements are conducted in MCS while the actual compensation application is in PCS, the geometric error models should be mapped from MCS to PCS and then substituted into the volumetric error model.

As shown in Fig. 13, the laser interferometer is aligned near the centerline of the ball screw to reduce the Abbe errors. First the axis is moved to the end of the stroke, then the laser interferometer is fixed on the slide or table close to the stroke endpoint and measurements are collected.

As shown in Fig. 14, the error measurements are conducted in MCS. The axis is moved from one end (Point A) to the other (Point B), and the errors are measured along the axis relative to the Point A. The errors captured by the laser interferometer are fitted to a

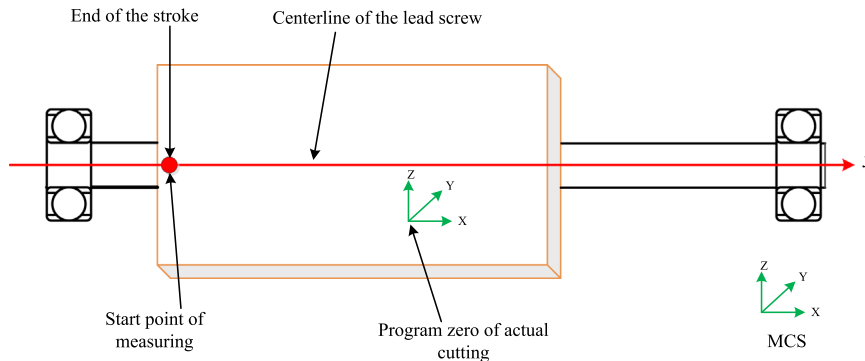


Fig. 13. Set up to reduce Abbe error during measurements.

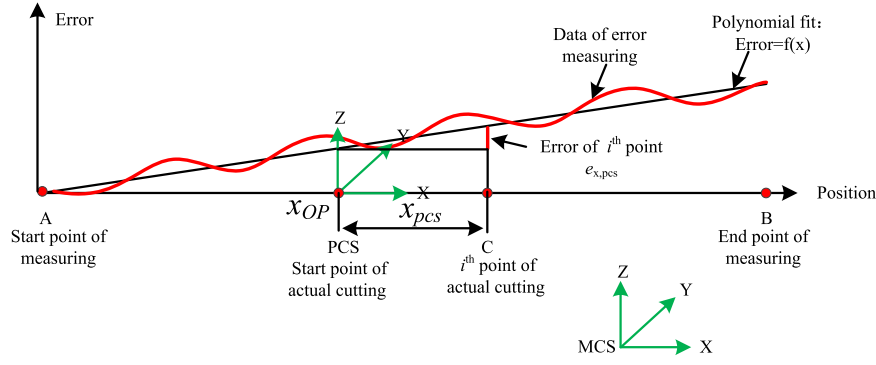


Fig. 14. Error mapping from Machine Coordinate System (MCS) to Part Coordinate System (PCS).

third order polynomial as a function of axis position x_m in MCS as:

$$\text{error} = f(x_m) \quad (32)$$

When the part is placed in the workspace of the machine, the part error at its coordinate center OP is zero, although machine has non-zero error ($\text{error}_{OP,MCS} = f(x_{OP})$) relative to its coordinate system (MCS). The objective is to compensate the machine errors along the tool path on the part by considering the location of the tool. If the tool is at position x_{pcs} relative to PCS whose center is x_{OP} , the error at the tool center point in MCS becomes:

$$e_{x,MCS} = f(x_m) \quad \leftarrow x_m = x_{OP} + x_{pcs} \quad (33)$$

However, the actual error on the part at its coordinate system (PCS) is evaluated as:

$$e_{x,PCS} = f(x_{OP} + x_{pcs})_{MCS} - f(x_{OP})_{MCS} \quad (34)$$

This mapping of error from MCS to PCS is carried out for all translational and angular motions along the tool path before compensating them correctly within the CNC.

After mapping all the geometric error models from MCS to PCS, they are fitted to polynomials and substituted into the volumetric error model (Step 5), which leads to the translational ($\Delta x, \Delta y, \Delta z$) and orientation ($\Delta I, \Delta J, \Delta K$) errors (Eq. (30)), and the compensated trajectory P_c (Eq. (31)). P_c is passed through the inverse kinematics of the machine to generate drive commands with geometric error compensation components ($x_c, y_c, z_c, \theta_{A_c}, \theta_{C_c}$) (Step 8).

5.2. Inverse kinematics for rotary and translational axes

The tool orientation ($\mathbf{O} = [I \ J \ K]^T$) is achieved by commanding angular positions (θ_A, θ_C) to 2 rotary drives (A,C), which are evaluated from the following inverse kinematics model. The orientation of the tool tip relative to the workpiece $\mathbf{O} = [I \ J \ K]^T$ is

expressed as a function of drive positions in PCS as:

$$\begin{bmatrix} \mathbf{O} \\ 0 \end{bmatrix} = g_{wt}(x, y, z, a, c)_{PCS} \begin{bmatrix} \mathbf{r}_{ot} \\ 0 \end{bmatrix} \quad (35)$$

where, $\mathbf{r}_{ot} = [0 \ 0 \ 1]^T$. The orientation of the tool is only determined by the rotary axes, and it is independent of translational movements. Hence Eq. (35) can be simplified as:

$$\begin{bmatrix} \mathbf{O} \\ 0 \end{bmatrix} = e^{\hat{\xi}_C \cdot \theta_C} \cdot e^{\hat{\xi}_A \cdot \theta_A} \begin{bmatrix} \mathbf{r}_{ot} \\ 0 \end{bmatrix} \quad (36)$$

Since the twists (ξ_A, ξ_C) are defined in Eq. (3), the corresponding rotary drive positions (θ_A, θ_C) can be extracted using the Paden-Kahan sub-problems of the screw theory as explained in [3,22]. The derivation process is briefly demonstrated here. Eq. (36) can be transformed as:

$$e^{\hat{\xi}_A \cdot \theta_A} \begin{bmatrix} \mathbf{r}_{ot} \\ 0 \end{bmatrix} = \mathbf{c} = e^{\hat{\xi}_C \cdot (-\theta_C)} \begin{bmatrix} \mathbf{O} \\ 0 \end{bmatrix} \quad (37)$$

The vector \mathbf{c} has the following relationship with 3 coefficients α, β and γ , which can be calculated with $\mathbf{u} = \mathbf{r}_{ot}$, $\mathbf{v} = \mathbf{O}$.

$$\mathbf{c} = \alpha \boldsymbol{\omega}_C + \beta \boldsymbol{\omega}_A + \gamma (\boldsymbol{\omega}_C \times \boldsymbol{\omega}_A) \quad (38)$$

$$\left. \begin{aligned} \alpha &= \frac{(\boldsymbol{\omega}_C^T \boldsymbol{\omega}_A) \boldsymbol{\omega}_A^T \mathbf{u} - \boldsymbol{\omega}_C^T \mathbf{v}}{(\boldsymbol{\omega}_C^T \boldsymbol{\omega}_A)^2 - 1}, \beta = \frac{(\boldsymbol{\omega}_C^T \boldsymbol{\omega}_A) \boldsymbol{\omega}_C^T \mathbf{v} - \boldsymbol{\omega}_A^T \mathbf{u}}{(\boldsymbol{\omega}_C^T \boldsymbol{\omega}_A)^2 - 1} \\ \gamma &= \pm \sqrt{\frac{\|\mathbf{u}\|^2 - \alpha^2 - \beta^2 - 2\alpha\beta \boldsymbol{\omega}_C^T \boldsymbol{\omega}_A}{\|\boldsymbol{\omega}_C \times \boldsymbol{\omega}_A\|^2}} \end{aligned} \right\} \quad (39)$$

Equations $e^{\hat{\xi}_A \cdot \theta_A} \cdot \mathbf{u} = \mathbf{c}$ and $e^{\hat{\xi}_C \cdot (-\theta_C)} \cdot \mathbf{v} = \mathbf{c}$ can be solved by using Paden-Kahan sub-problem 1 shown as:

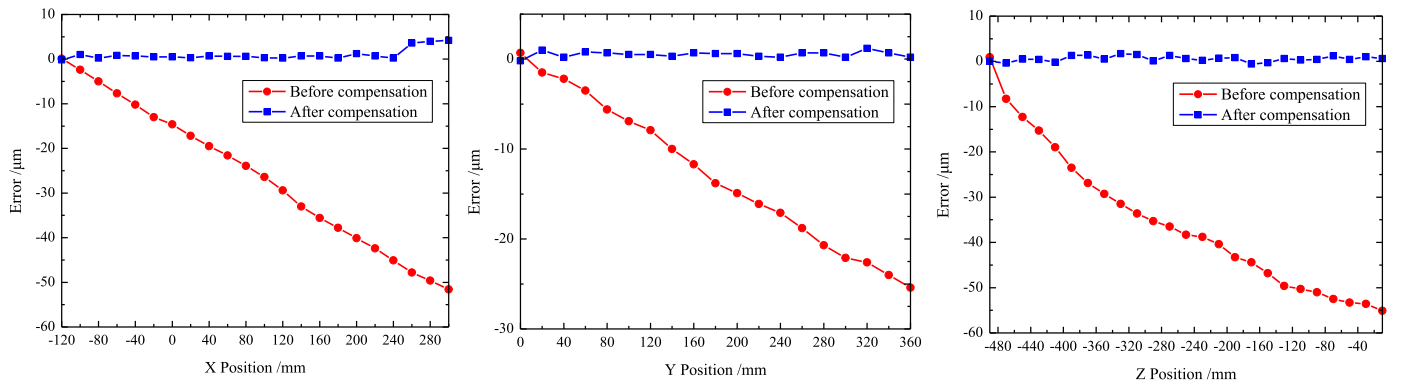


Fig. 15. Experimental results of error compensation for linear axes.

Table 3

Experimental parameters of axial ballbar measurements for rotary axes.

Axis name	L (mm)	H (mm)	Axis travel	Initial position of table-side ball in MCS (mm)	Initial position of spindle-side ball in MCS (mm)
A-axis	0	49.770	30° → -60°	(0,24.885, -456.237)	(100,24.885, -456.237)
C-axis	100	49.490	0° → 360°	(100,0, -449.849)	(100,0, -349.849)

$$\left. \begin{aligned} \mathbf{u}' &= \mathbf{u} - \boldsymbol{\omega}_A \cdot \boldsymbol{\omega}_A^T \cdot \mathbf{u}, \mathbf{c}' = \mathbf{c} - \boldsymbol{\omega}_A \cdot \boldsymbol{\omega}_A^T \cdot \mathbf{c} \\ \theta_A &= a \tan 2\left(\boldsymbol{\omega}_A^T(\mathbf{u}' \times \mathbf{c}'), \mathbf{u}'^T \mathbf{c}'\right) \end{aligned} \right\} \quad (40)$$

$$\left. \begin{aligned} \mathbf{v}' &= \mathbf{v} - \boldsymbol{\omega}_C \cdot \boldsymbol{\omega}_C^T \cdot \mathbf{v}, \mathbf{c}' = \mathbf{c} - \boldsymbol{\omega}_C \cdot \boldsymbol{\omega}_C^T \cdot \mathbf{c} \\ \theta_C &= -a \tan 2\left(\boldsymbol{\omega}_C^T(\mathbf{v}' \times \mathbf{c}'), \mathbf{v}'^T \mathbf{c}'\right) \end{aligned} \right\} \quad (41)$$

If the tool tip position is defined by vector $\mathbf{P} = [X \ Y \ Z]^T$, it corresponds to the coordinates of 3 translational and 2 rotary drives as:

$$\begin{aligned} \begin{bmatrix} \mathbf{P} \\ 1 \end{bmatrix} &= \mathbf{g}_{wt}(x, y, z, \theta_A, \theta_C) \begin{bmatrix} 0 \\ 0 \\ 0 \\ 1 \end{bmatrix} = \mathbf{g}^{-1}_{bw}(0) \cdot e^{\hat{\xi}_C \cdot \theta_C} \cdot e^{\hat{\xi}_A \cdot \theta_A} \cdot e^{\hat{\xi}_X \cdot x} \cdot e^{\hat{\xi}_Y \cdot y} \cdot e^{\hat{\xi}_Z \cdot z} \cdot \mathbf{g}_{bt}(0) \\ &= \mathbf{g}^{-1}_{bw}(0) \cdot e^{\hat{\xi}_C \cdot \theta_C} \cdot e^{\hat{\xi}_A \cdot \theta_A} \cdot \left(\begin{bmatrix} 1 & 0 & 0 & 0 \\ 0 & 1 & 0 & 0 \\ 0 & 0 & 1 & 0 \\ 0 & 0 & 0 & 1 \end{bmatrix} + \begin{bmatrix} 0 & 0 & 0 & x \\ 0 & 0 & 0 & y \\ 0 & 0 & 0 & z \\ 0 & 0 & 0 & 0 \end{bmatrix} \right) \cdot \mathbf{g}_{bt}(0) \cdot \begin{bmatrix} 0 \\ 0 \\ 0 \\ 1 \end{bmatrix} \end{aligned} \quad (42)$$

Substituting the evaluated positions of the rotary drives (θ_A, θ_C) into Eq. (42), the positions (x, y, z) of 3 translational drives are solved from the inverse kinematics model as:

$$\begin{bmatrix} x \\ y \\ z \\ 0 \end{bmatrix} = e^{\hat{\xi}_A \cdot (-\theta_A)} \cdot e^{\hat{\xi}_C \cdot (-\theta_C)} \cdot \mathbf{g}_{bw}(0) \begin{bmatrix} \mathbf{P} \\ 1 \end{bmatrix} - \mathbf{g}_{bt}(0) \begin{bmatrix} 0 \\ 0 \\ 0 \\ 1 \end{bmatrix} \quad (43)$$

In summary, the tool tip position and tool orientation ($[X \ Y \ Z \ I \ J \ K]^T$) are transformed to drive positions $[x \ y \ z \ \theta_A \ \theta_C]^T$ with the inverse kinematic model of the machine.

6. Simulation and experimental results

Compensation experiments have been conducted on a five-axis machine (Quaser UX600) controlled by a Heidenhein iTNC530 CNC. The 3 translational and 2 rotary axes have been compensated by entering look-up tables into the CNC. As shown in Fig. 15, the positioning errors of the X, Y and Z drives are reduced from (50, 25, 55 μm) to (5, 1, 2 μm), respectively.

After completely compensating the positioning errors of 3 translational axes (Fig. 15), 20 errors of 2 rotary axes have been measured with ballbar tests (Fig. 9) using the parameters listed in Table 3. Here the axial measurements are analyzed as an example.

Substituting the 20 identified error parameters of the rotary axes (Fig. 11 and Fig. 12) into Eq. (17), the position of the table-side ball O_1 in MCS can be obtained. When conducting ballbar tests, the Rotation Tool Center Point function is turned on. Translational axes follow the rotation automatically, and they follow the circular motion so that the spindle-side ball O_2 is kept stationary to the table-side ball O_1 . For the axial measurement of the C-axis, the position of the spindle-side ball O_2 in MCS is decided by the X- and Y-axis as:

$$\mathbf{O}_2 = \begin{pmatrix} e^{\hat{\xi}_{eY} \cdot \theta_{eY}} \cdot e^{\hat{\xi}_{eY} \cdot y} \cdot e^{\hat{\xi}_{eY}^D \cdot \theta_{eY}} \cdot \begin{pmatrix} e^{\hat{\xi}_X \cdot (-x)} \cdot e^{\hat{\xi}_{eX}^D \cdot \theta_{eX}} \end{pmatrix} \cdot \begin{bmatrix} 100 \\ 0 \\ -349.849 \\ 1 \end{bmatrix} \end{pmatrix} \quad (44)$$

The distance between the balls O_1 and O_2 is the ballbar length and the measured error can be evaluated as:

$$\rho = \sqrt{\|\mathbf{O}_1 - \mathbf{O}_2\|} - l \quad (45)$$

where l is the reference length of the ballbar. However, the commercial CNC compensates only 3 linear ($\delta_{xx}, \delta_{yy}, \delta_{zz}$) and 2 angular positioning ($\varepsilon_{xa}, \varepsilon_{zc}$) errors but not all 41 errors, hence there is not much improvement in the accuracy of rotary drives (Fig. 16a–b). To verify the proposed volumetric error model, the simulated ballbar results (uncompensated) are compared with the real measurements (uncompensated) in Fig. 16. The simulated ballbar results can be calculated by Eqs. (17), (44) and (45). Fig. 17 shows the differences between the ballbar measurements and the simulated results for uncompensated rotary drives. The sources of errors in the prediction are due to the identification inaccuracy of 20 geometric errors of the rotary axes, servo mis-match and the influence of gravity on the ballbar measurements.

If we assume that the geometric errors are modeled and measured accurately, all 41 errors can be compensated to improve the accuracy of the machine which is demonstrated in simulations for 2 rotary drives (Fig. 16c–d).

The full compensation has been demonstrated on a virtual five-axis CNC platform [30] by simultaneously considering all 41 errors. The compensated and uncompensated tool tip positions and tool axis orientations along a helical tool path are shown in Fig. 18. To clearly show the volumetric errors and the compensation results, some relatively large geometric errors were deliberately substituted into the forward kinematics model. The total position error is reduced from 5 mm to 10 μm after 2 iterations. The reference tool path shows the ideal tool path without considering any geometric error, while the simulated tool path presents the one with geometric errors.

For real cases, all the component errors of the five axes were measured by the laser interferometer and the ballbar. Among these errors, the position dependent errors were mapped from MCS to PCS, fitted by third order polynomials and then substituted into the volumetric error model (Section 5.1) embedded in the Virtual CNC system. The final contouring error of the tool path mainly comes from the servo dynamics and the volumetric errors. A partial enlarged view is shown in Fig. 19, and it can be found that before compensation, the total contouring error of the final tool path is as large as 60 μm , but is reduced to 7 μm after volumetric error compensation. The orientation errors are also fully compensated.

7. Conclusion

This paper presents a systematic modeling, measurement and compensation of both position-independent and position-dependent geometric errors of five-axis CNC machines. When the measured errors of 2 rotary drives (i.e. with a ballbar) are decoupled into 12 position-dependent and 8 position-independent geometric

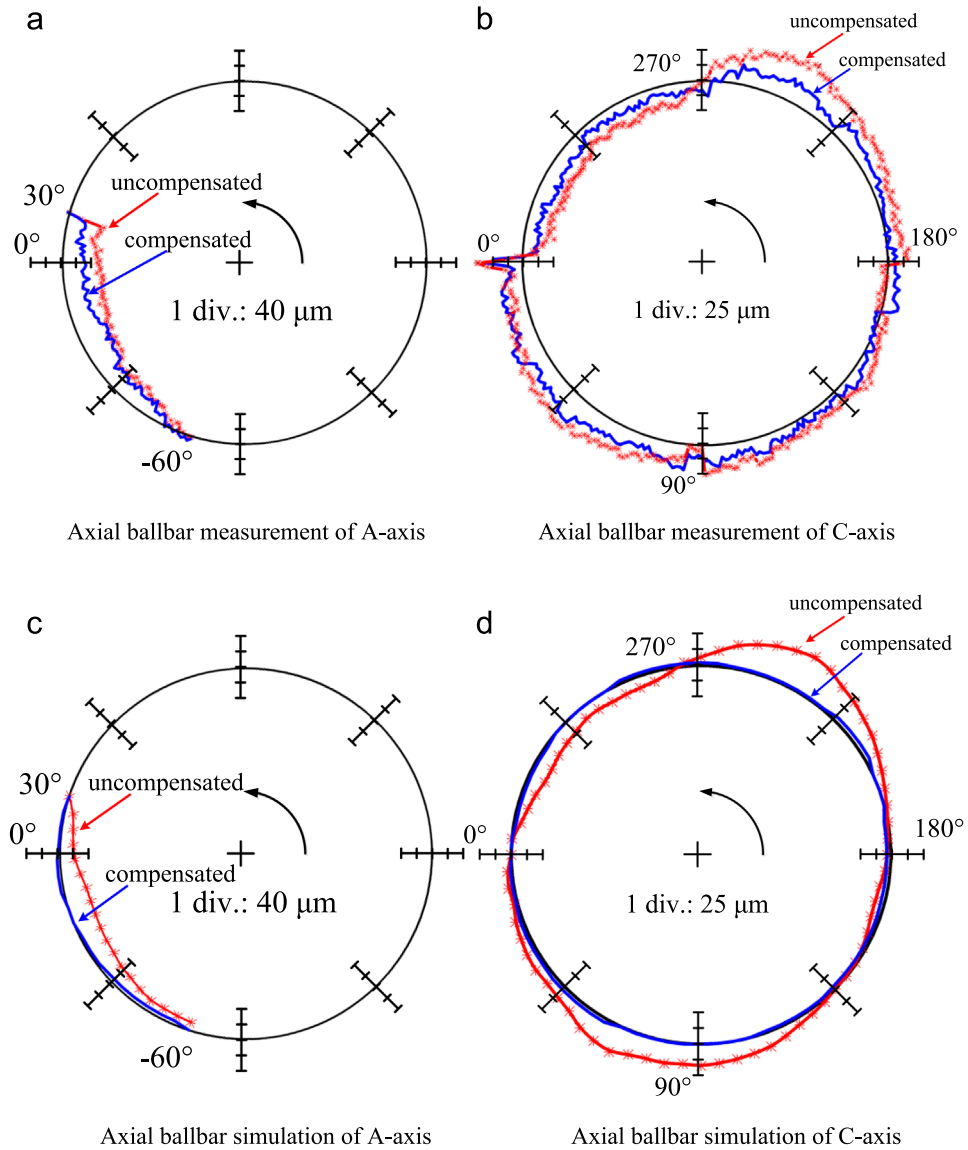


Fig. 16. Error compensation of rotary axes. (a)(b) ballbar measurements before and after compensating angular positioning errors with CNC, (c)(d) Simulated results before and after compensating all 41 errors.

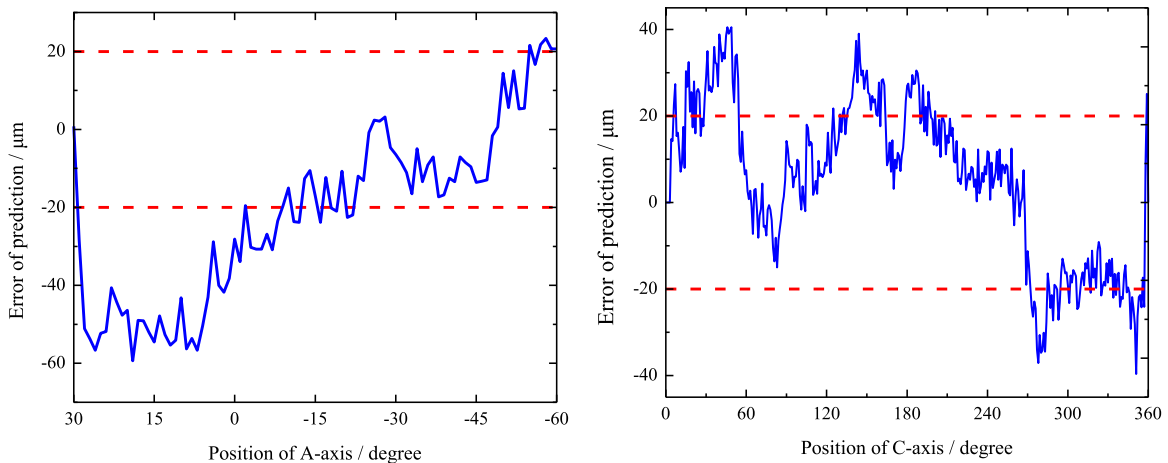


Fig. 17. The error between the measured and predicted ballbar results for two rotary drives.

errors, they can be combined with the 21 geometric errors of translational axes directly measured with a laser interferometer. The 41 decoupled geometric errors are mapped into error twists,

which facilitates the calculation of not only the volumetric error of the machine at any position, but their compensation in the CNC by employing the kinematic model of the five-axis machine. The

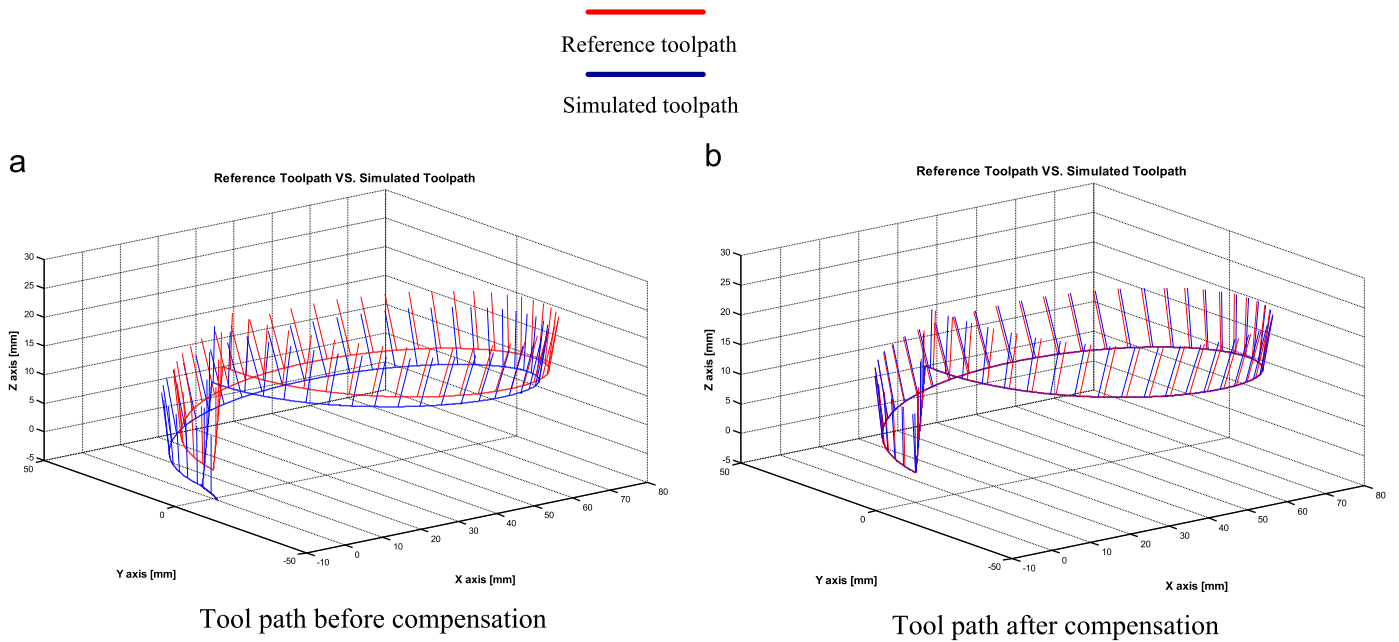


Fig. 18. Helix tool path before and after compensation with large errors.

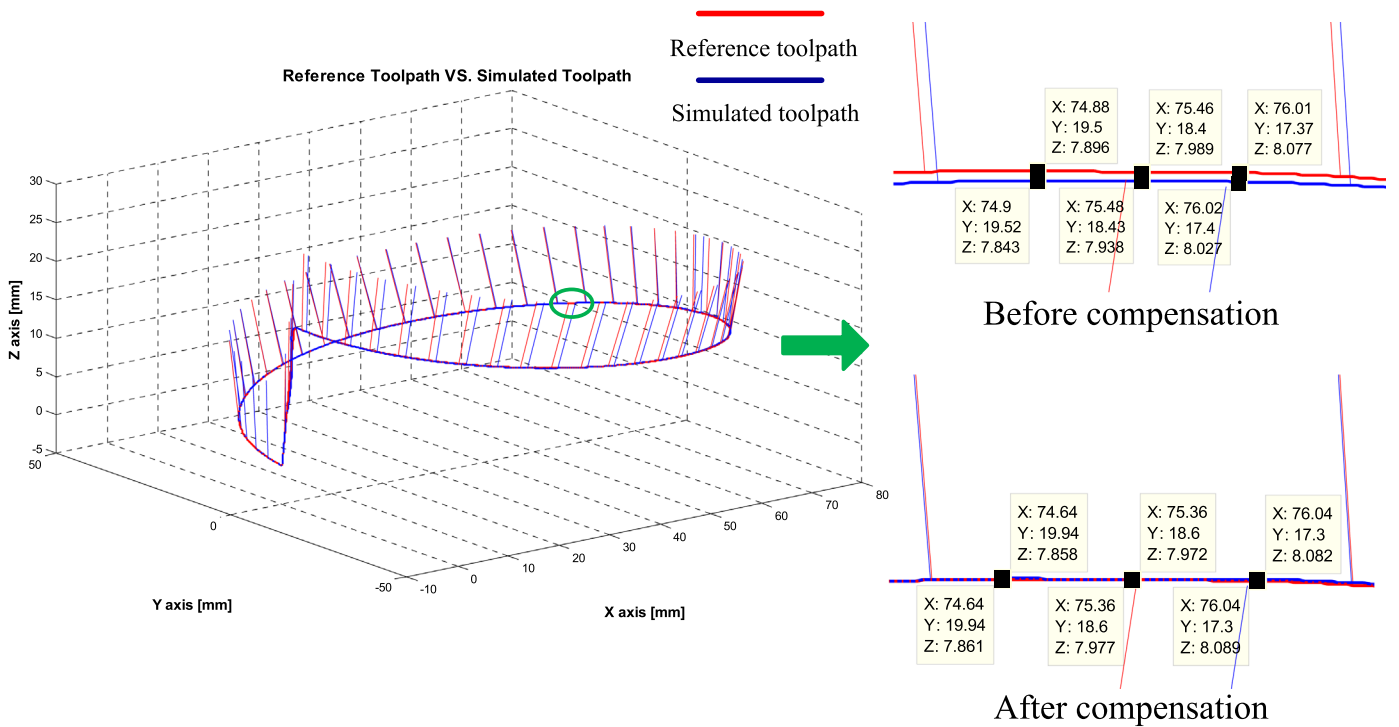


Fig. 19. Partial enlarged view before and after compensation.

current commercial CNCs, which only allow for the compensation of error at each discrete position through look-up tables, can integrate the proposed strategy to predict the geometric errors of the machine at any position along the tool path and compensate them in real time. The proposed concept has been demonstrated in an open five-axis virtual CNC system built in-house.

The proposed research can be extended to include measurement uncertainties and the inclusion of thermal deformations of the machine.

Acknowledgments

This research was sponsored by the NSERC (NSERC IRC J 260683)-Pratt & Whitney Canada Research Chair, the China Scholarship Council (No. 201406230151), and National Natural Science Foundation projects of the People's Republic of China 51275305, the Shanghai Municipality Military and Civilian Projects for the Construction of Industrial Development System [No. JMJH2013002], the Liaoning Province Scientific and Technical

Innovation Key Special Projects [No. 201301001] and the Shanghai Municipality Minhang District Industry-University-Research Cooperation Projects [No. 2013MH111].

References

- [1] A.C. Okafor, Y.M. Ertekin, Derivation of machine tool error models and error compensation procedure for three axes vertical machining center using rigid body kinematics, *Int. J. Mach. Tools Manuf.* 40 (2000) 1199–1213.
- [2] L. Uriarte, M. Zatarain, D. Axinte, J. Yagüe-Fabra, S. Ihlenfeldt, J. Eguia, A. Olarra, Machine tools for large parts, *CIRP Ann. – Manuf. Technol.* 62 (2013) 731–750.
- [3] J. Yang, Y. Altintas, Generalized kinematics of five-axis serial machines with non-singular tool path generation, *Int. J. Mach. Tools Manuf.* 75 (2013) 119–132.
- [4] S.K. Moon, Y.M. Moon, S. Kota, et al., Screw theory based metrology for design and error compensation of machine tools. *Proc. DETC 1* (2001) 697–707.
- [5] G. Fu, J. Fu, Y. Xu, Z. Chen, Product of exponential model for geometric error integration of multi-axis machine tools, *Int. J. Adv. Manuf. Technol.* 71 (9–12) (2014) 1653–1667.
- [6] W. Tian, W. Gao, D. Zhang, T. Huang, A general approach for error modeling of machine tools, *Int. J. Mach. Tools Manuf.* 79 (2014) 17–23.
- [7] H. Schwenke, W. Knapp, H. Haitjema, A. Weckenmann, R. Schmitt, F. Delbressine, Geometric error measurement and compensation of machines – an update, *CIRP Ann. – Manuf. Technol.* 57 (2008) 660–675.
- [8] S. Ibaraki, W. Knapp, Indirect measurement of volumetric accuracy for three-axis and five-axis machine tools: a review, *Int. J. Autom. Technol.* 6 (2) (2012) 110–124.
- [9] M. Tsutsumi, A. Saito, Identification and compensation of systematic deviations particular to 5-axis machining centers, *Int. J. Mach. Tools Manuf.* 43 (2003) 771–780.
- [10] C. Hong, S. Ibaraki, Non-contact *R*-test with laser displacement sensors for error calibration of five-axis machine tools, *Precis. Eng.* 37 (2013) 159–171.
- [11] S. Ibaraki, C. Oyama, H. Otsubo, Construction of an error map of rotary axes on a five-axis machining center by static *R*-test, *Int. J. Mach. Tools Manuf.* 51 (2011) 190–200.
- [12] S. Ibaraki, T. Iritani, T. Matsushita, Calibration of location errors of rotary axes on five-axis machine tools by on-the-machine measurement using a touch-trigger probe, *Int. J. Mach. Tools Manuf.* 58 (2012) 44–53.
- [13] M. Givi, J.R.R. Mayer, Validation of volumetric error compensation for a five-axis machine using surface mismatch producing tests and on-machine touch probing, *Int. J. Mach. Tools Manuf.* 87 (2014) 89–95.
- [14] S. Ibaraki, Y. Ota, A machining test to calibrate rotary axis error motions of five-axis machine tools and its application to thermal deformation test, *Int. J. Mach. Tools Manuf.* 86 (2014) 81–88.
- [15] S. Ibaraki, T. Kudo, T. Yano, T. Takatsuji, S. Osawa, O. Sato, Estimation of three-dimensional volumetric errors of machining centers by a tracking interferometer, *Precis. Eng.* 39 (2015) 179–186.
- [16] S. Ibaraki, K. Nagae, G. Sato, Proposal of “open-loop” tracking interferometer for machine tool volumetric error measurement, *CIRP Ann. – Manuf. Technol.* 63 (2014) 501–504.
- [17] W.T. Lei, Y.Y. Hsu, Accuracy enhancement of five-axis CNC machines through real-time error compensation, *Int. J. Mach. Tools Manuf.* 43 (2003) 871–877.
- [18] Y.Y. Hsu, S.S. Wang, A new compensation method for geometry errors of five-axis machine tools, *Int. J. Mach. Tools Manuf.* 47 (2007) 352–360.
- [19] S.W. Zhu, G.F. Ding, S.F. Qin, J. Lei, L. Zhuang, K.Y. Yan, Integrated geometric error modeling, identification and compensation of CNC machine tools, *Int. J. Mach. Tools Manuf.* 52 (2012) 24–29.
- [20] N. Huang, Y. Jin, Q. Bi, Y. Wang, Integrated post-processor for 5-axis machine tools with geometric errors compensation, *Int. J. Mach. Tools Manuf.* 94 (2015) 65–73.
- [21] J. Yang, J.R.R. Mayer, Y. Altintas, A position independent geometric errors identification and correction method for five-axis serial machines based on screw theory, *Int. J. Mach. Tools Manuf.* 95 (2015) 52–66.
- [22] R.M. Murray, Z.X. Li, S.S. Sastry, *A Mathematical Introduction to Robotic Manipulation*, CRC Press, Florida, 1994.
- [23] ISO-230-7:2006, Test code for machine tools –Part 7: Geometric accuracy of axes of rotation.
- [24] E.L.J. Bohez, Five-axis milling machine tool kinematic chain design and analysis, *Int. J. Mach. Tools Manuf.* 42 (4) (2002) 505–520.
- [25] ISO/DIS 10791-6:2014, Test conditions for machining centers–Part 6: Accuracy of speeds and interpolations.
- [26] M. Tsutsumi, S. Tone, N. Kato, R. Sato, Enhancement of geometric accuracy of five-axis machining centers based on identification and compensation of geometric deviations, *Int. J. Mach. Tools Manuf.* 68 (2013) 11–20.
- [27] S. Xiang, J. Yang, Y. Zhang, Using a double ball bar to identify position-independent geometric errors on the rotary axes of five-axis machine tools, *Int. J. Adv. Manuf. Technol.* 70 (9–12) (2014) 2071–2082.
- [28] S. Xiang, J. Yang, Using a double ball bar to measure 10 position-dependent geometric errors for rotary axes on five-axis machine tools, *Int. J. Adv. Manuf. Technol.* 75 (2014) 559–572.
- [29] Y. Altintas, *Manufacturing Automation: Metal Cutting Mechanics, Machine Tool Vibrations, and CNC Design*, Cambridge University Press, Cambridge, United Kingdom, 2012.
- [30] Y. Altintas, S. Tulsyan, Prediction of part machining cycle times via virtual CNC, *CIRP Ann. – Manuf. Technol.* 64 (2015) 361–364.